POLITECNICO DI TORINO
Repository ISTITUZIONALE

Upcycled cellulose pulp from local agricultural waste as a crosslinker in one-pot DLP-printable formulations for ionic wearable sensors

Original
Upcycled cellulose pulp from local agricultural waste as a crosslinker in one-pot DLP-printable formulations for ionic wearable sensors / Vittoria Piras, M., Mogli, G., Corrias, F., Paniziutti, S., Frau, F., Sarais, G., Secci, F., Stassi, S., Chiappone, A.. - In: MATERIALS & DESIGN. - ISSN 0264-1275. - 270:(2026), pp. 1-14. [10.1016/j.matdes.2026.117016]

Availability:
This version is available at: 11583/3015668 since: 2026-09-17T09:54:44Z

Publisher:
Elsevier

Published
DOI:10.1016/j.matdes.2026.117016

Terms of use:

This article is made available under terms and conditions as specified in the corresponding bibliographic description in the repository

Publisher copyright

(Article begins on next page)

19 November 2026

Materials & Design 270 (2026) 117016

Contents lists available at ScienceDirect

Materials & Design

journal homepage: www.elsevier.com/locate/matdes

Upcycled cellulose pulp from local agricultural waste as a crosslinker in one-pot DLP-printable formulations for ionic wearable sensors

Maria Vittoria Piras [a], Giorgio Mogli [b], Francesco Corrias [c], Sara Paniziutti [a], Franco Frau [a], Giorgia Sarais [c], Francesco Secci [a], Stefano Stassi [b], Annalisa Chiappone [a,*]

[a] Dipartimento di Scienze Chimiche e Geologiche, Università degli Studi di Cagliari, Complesso Universitario di Monserrato, Monserrato (Cagliari), 09042, Italy
[b] Dipartimento di Scienza Applicata e Tecnologia, Politecnico di Torino, Turin 10129, Italy
[c] Dipartimento di Scienze della Vita e dell'Ambiente, Università degli Studi di Cagliari, Complesso Universitario di Monserrato, Monserrato (Cagliari), 09042, Italy

ARTICLE INFO

Keywords:
DLP printing
Bio-wastevalorization
Cellulose pulp
Eutectogel
Strain sensors

ABSTRACT

Strain-responsive materials are gaining attention for applications in wearable sensors and flexible electronics, driving the need for sustainable production methods. Herein, cellulose pulp (CP) was extracted from local agricultural waste and dispersed in a photopolymerizable deep eutectic solvent (DES) composed of a hydrated salt and acrylic acid. The treatment with this solvent enables the dispersion of CP with its simultaneous functionalization with acrylic moieties, making it an added-value crosslinker for the DES photopolymerization. The resulting dispersion is suitable for DLP 3D printing, thanks to the cellulose's crosslinking role and enables the production of 3D complex samples. The printed eutectogel boasts excellent ionic conductivity, and mechanical performance tailored for sensing applications with Gauge Factor of of 0.84 ± 0.04 and 1.45 ± 0.24 in the linear ranges between 0–50% and 50–200% respectively. The eutectogel exhibits exceptional sensitivity to both small (0.02%) and large (above 200%) deformations, that can be tuned through the interplay between the material intrinsic properties and 3D design and allows the device implementation in wearable sensors. Sensing performances are maintained for over twenty weeks, far beyond than the other reported works in cellulose based eutectogels. This work paves the way for the next generation of sustainable, high-performance, and customizable soft electronic materials, able to exploit and valorise local waste, entering the mindset of the circular economy.

1. Introduction

Highly deformable conductive materials are rapidly becoming key enablers for next-generation flexible electronics, wearable systems, soft robotics, and human–machine interfaces [1–3]. In these applications, materials are required to sustain repeated stretching, bending, and twisting while preserving stable electrical or ionic conductivity, mechanical integrity, and sensing reliability over time and across variable environmental conditions [4–7]. At the same time, the integration of additive manufacturing technologies, particularly vat-photopolymerization techniques, is redefining the design freedom of sensing devices, enabling the fabrication of complex architectures that synergistically combine geometry and material response to enhance sensitivity and signal resolution [8–10]. As wearable and soft electronic technologies continue to expand, however, the development of sustainable material platforms is becoming equally critical, demanding solutions that couple high performance with reduced environmental impact and circular-material strategies [11–13].

In this context, bio-based materials have emerged as promising candidates for the fabrication of sustainable strain sensors and printable soft devices [14–16]. Among them, cellulose has attracted enormous attention because of its abundance, renewability, low density, mechanical robustness, and intrinsic chemical versatility [17,18].

Different cellulose-based systems have been explored for conductive and stretchable applications, including hydrogels and organohydrogels containing cellulose nanofibers [19–23], nanofibrils [24], or bacterial cellulose [25–27] combined with conductive polymers or ionic/electronic fillers; in most of the cases cellulose was used in very low amounts (approximately 1 wt%); different strategies have also relied on water-soluble cellulose derivatives [28,29]. As an alternative approach, cellulose pulp could be solubilized or dispersed using Ionic Liquids (ILs) [30] and Deep Eutectic Solvents (DESs) [31–35], which are currently regarded among the most promising and sustainable media for cellulose processing. Among the different classes of DESs, hydrated metal salt

* Corresponding author.
E-mail address: annalisa.chiappone@unica.it (A. Chiappone).

https://doi.org/10.1016/j.matdes.2026.117016
Received 13 March 2026; Received in revised form 31 July 2026; Accepted 9 September 2026
Available online 14 September 2026
0264-1275/© 2026 The Author(s). Published by Elsevier Ltd. This is an open access article under the CC BY license (http://creativecommons.org/licenses/by/4.0/).

DESs based on $ZnCl_2$ and acidic components have demonstrated remarkable effectiveness for room-temperature cellulose dissolution and processing [33,36,37]. Beyond their solvent capability, these systems have recently attracted growing interest for the fabrication of highly stretchable eutectogels for strain sensing [38–43], owing to their intrinsic ionic conductivity, wide operating-temperature range, and excellent mechanical deformability [44–46]. Interestingly, similar DES formulations have also shown catalytic activity toward esterification and acylation reactions involving hydroxyl-rich substrates, including polysaccharides [36,47], as well as the ability to promote lignocellulosic fractionation through the selective solubilization of lignin and hemicellulose [48–50]. Collectively, these observations suggest that hydrated $ZnCl_2$-based DESs may play a dual role during cellulose processing. On one hand, the dynamic coordination chemistry of Zn(II), combined with the extensive hydrogen-bonding interactions established by water and the hydrogen-bond donor, can disrupt the native intermolecular hydrogen-bond network of cellulose, promoting fibre swelling, aggregate disassembly and partial solubilization, acting as a Hydrogen bond Scissor (HBS). On the other hand, the Lewis acidic character of Zn^{2+} may activate carboxylic acids toward esterification of the newly accessible cellulose hydroxyl groups. We therefore hypothesized that a $ZnCl_2$/H_2O/acrylic acid DES could simultaneously act as an efficient cellulose-processing medium and as a reactive solvent capable of directly generating acrylic-functionalized cellulose in a single step, eliminating the need for separate dissolution and chemical modification processes.

Building on these advances and aiming to move a step further toward sustainable printable electronics, herein we introduce a multifunctional strategy that simultaneously addresses biomass valorization, cellulose processing, chemical functionalization, and additive manufacturing within a single platform. Specifically, cellulose pulp (CP) was extracted from dry olive leaves, an abundant local agricultural waste, and dispersed in a hydrated metal salt/acrylic acid eutectic system specifically optimized for cellulose processing. Remarkably, the eutectic medium plays a dual role: it promotes the effective dispersion/partial solubilization of cellulose while concurrently enabling the grafting of acrylic functionalities onto the cellulose structure. This one-pot approach results in a photocurable formulation directly suitable for vat-photopolymerization printing upon the addition of a photoinitiator, eliminating the need for separate cellulose modification steps.

The developed strategy, schematically illustrated in Fig. 1a, enables the fabrication of ionically conductive eutectogel with complex three-dimensional geometries, high deformability, and long-term mechanical, electrical and functional stability, employing cellulose concentrations that exceed most of the reported cellulose-containing eutectogels [40,41,51,52]. Importantly, the covalent incorporation of acrylic-modified cellulose within the polymeric network generates

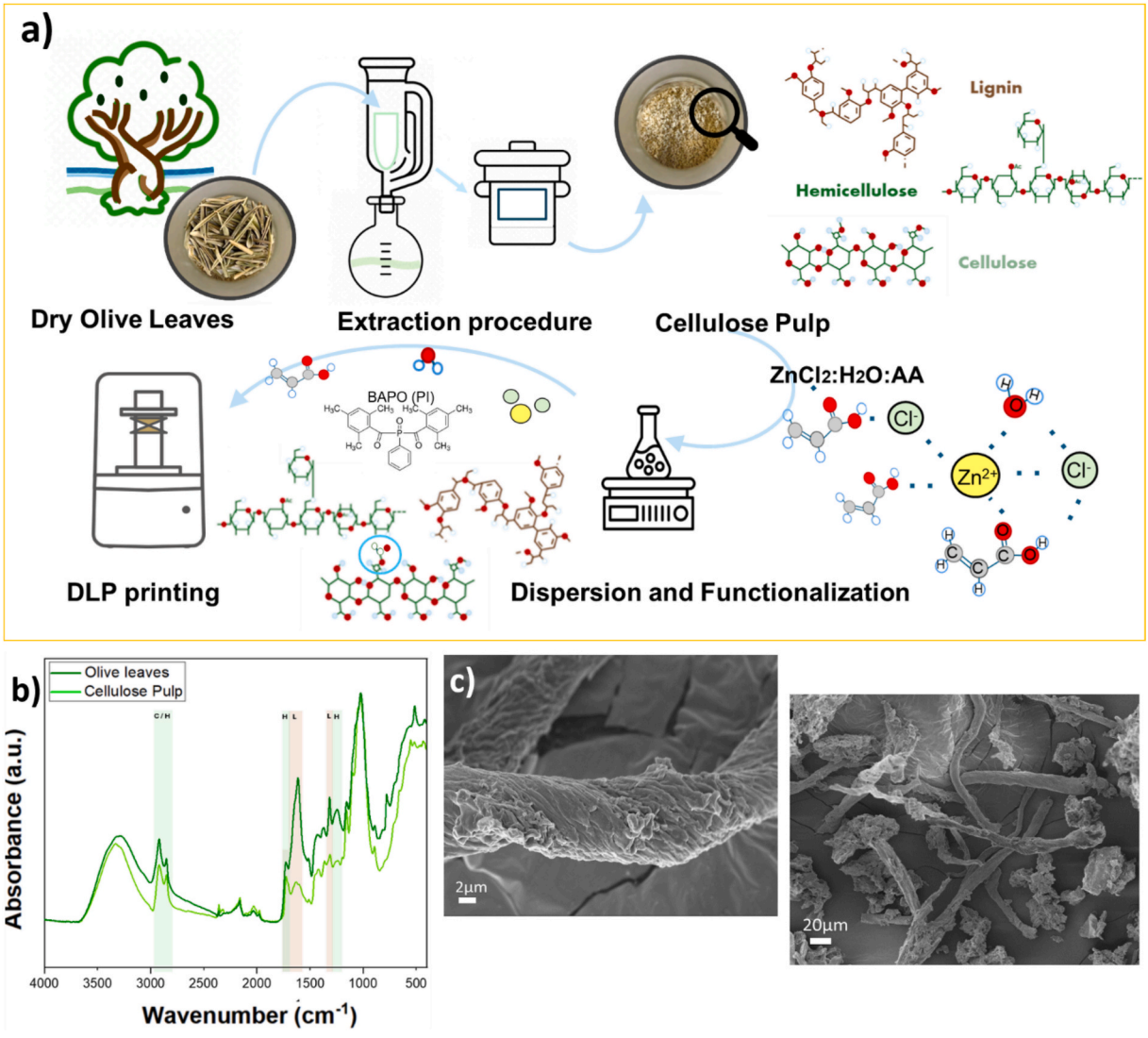


Fig. 1. (a) Schematic representation of the development of the one-pot formulation for DLP printing obtained using cellulose pulp extracted from local agricultural waste; (b) IR spectra of the extracted cellulose pulp compared with Olive leaves powder; (c) SEM images of the extracted cellulose pulp.

structurally stable eutectogels compatible with Digital Light Processing (DLP) printing, overcoming the limitations associated with non-crosslinked linear systems that would otherwise dissolve in the liquid resin during printing. The possibility to combine tailored architectures with conductive and stretchable eutectogels allows the creation of conformable sensing devices in which geometry and material properties synergistically enhance strain sensitivity and signal response.

The novelty of this work lies in the convergence of multiple aspects that are rarely integrated within a single material platform. By combining waste-derived cellulose, reactive eutectic chemistry, and additive manufacturing, this work demonstrates a scalable route toward sustainable, high-performance strain-sensing materials for wearable technologies and soft electronics. The integration of customized 3D architectures with deformability, conductivity, sensitivity, and long-term operational stability [53,54] opens new opportunities for the development of environmentally responsible sensing platforms with enhanced functionality and user adaptability.

2. Materials and methods

2.1. Materials

Olive leaves were harvested in sud-Sardinian olive groves from *Olea Europaea* plants. Acrylic Acid, Zinc Cloride, Phenylbis(2,4,6-trimethylbenzoyl)phosphine oxide (BAPO), Ethanol, sulfuric acid, sodium hydroxide and hydrochloric acid were purchased from Merck and used as received.

2.2. Olive leaves treatment and cellulose extraction

The extraction procedure was modified form [55], avoiding the bleaching step. In detail, Olive leaves were cut into small pieces (ca. 2 × 2 mm^2), dried and grinded to produce homogeneous powders with a diameter of about 250 μm. The powder was then subjected to Soxhlet extraction using ethanol to remove the lipidic fraction, chlorophylls, and the full range of bioactive compounds, characteristic of olive leaves. Subsequently, the powder (~15 g) was subjected solvothermal hydrolysis to extract most of the lignocellulosic materials from cellulose. This process was performed in an autoclave (Teflon autoclave with a steel jacket, 300 mL) using a 1:1 H_2O-EtOH mixture (90 mL) in the presence of sulfuric acid (0.05 M) at 150 °C for 6 h. After returning to room temperature, the solid was filtered and washed with hot distilled water. The filtered solid was then dried under an IR lamp for 2 h. The obtained powder was suspended in an aqueous solution of 6% HCl and stirred at 80 °C for 1 h to depolymerize the cellulose chain and reduce the residual bonds between cellulose and lignin and hemicellulose. This procedure allowed us to obtain about 2.4 g of material (yield on the total leaves weight: 14%, yield on the leaf fibrous fraction: 35%). After that, the suspension was neutralized by adding dropwise an aqueous solution of NaOH until pH 7 was reached. The resulting media was left to rest for 10 h at room temperature to allow Cellulose precipitation. The cellulose-based powder was filtered and washed with ethanol and dried under vacuum at 60 °C for 10 h.

2.3. Cellulose pulp dispersion and functionalization

CP was added in a eutectic mixture made of Zinc Chloride, H_2O and Acrylic Acid. Firstly, the eutectic mixture was prepared, (preliminary characterizations were performed on the DES solutions, as detailed below) and subsequently the cellulose-based powder was added slowly and with constant agitation. The reaction mixture was stirred overnight at room temperature. Finally, the mixture was stirred at 70 °C for 4 h.

Various concentrations of the mixture $ZnCl_2/H_2O$/AA were tested, respectively 1:1:2, 1:1:2.5, 1:1:3, 1:1:3.5 and 1:1:4 M ratio. The prepared samples are summarized in Table S1. The 1:1:3 was selected as the best based on rheological and photorheological data. When photorheology tests were performed 1 wt% of BAPO photoinitiator was always added to the formulation. In addition, the amount of cellulose relative to the eutectic mixture 1:1:3 was adjusted, aiming to increase the cellulose-based powder content rather than the acid, attempting 0, 3%,6% and 9%. The 6% percentage was selected as the best based on the obtained data.

2.4. Preparation of photocurable formulations and DLP printing

The mixture based on DES 1:1:3 and 6 wt% of CP was prepared and, subsequently 1 wt% of BAPO was added and stirred for 30 min. The mixture was polymerized, and 3D printed with DLP, using an ASIGA UV-MAX X27 DLP printer (XY pixel resolution of 27 μm; diode source emitting at 385 nm). Different 3D models were designed, using Solidworks 2019 CAD software, converted to STL file formats, and 3D-printed. The printing parameters are detailed in the Supporting Information file.

2.5. Characterizations

Olive leaves composition:

Preliminary tests performed on olive leaves including Moisture and ashes quantification, total lipids quantification and fibrous content composition determination are described in detail in the Supplementary information file. Briefly, moisture and ashes were quantified gravimetrically after carbonization. Total lipids were determined according to a modified Folch method. While the for the determination of the composition of the *Fibrous fraction, m*atrix samples were analysed for acid detergent fiber (ADF), neutral detergent fiber (NDF), and acid detergent lignin (ADL) according to Van Soest et al. using a FIWE Advance Automatic Fiber Analyzer (VELP).

FTIR-ATR: Infrared spectra were collected using a Jasco FTIR-4XLE Spectrometer equipped with ATR tool, 64 scans were collected with a resolution of 4 cm^{-1} from 4000 to 400 cm^{-1}.

^{13}C CP/MAS NMR: spectra were recorded on a Bruker Avance III HD at 5 kHz rotation, contact time: 2 ms, delay: 3, line broadening: 10 Hz.

TGA: Thermogravimetrical analysis were performed placing about 8 mg of sample in alumina pans with nitrogen flux of 40 mL min^{-1} and heating from 30 to 800 °C at a rate of 10 K min^{-1}.

SEM: The morphological characterization of the cellulose pulp was performed by using an FESEM Zeiss Supra 40 after metallization of the samples with a 7 nm thick film of platinum.

Rheological measurements: Viscosity and photorheology tests were performed using a Physica MCR 302, Anton Paar rheometer in the parallel plate mode. Viscosity measurements were performed in flow, setting a shear rate ramp between 0.1 and 100 s^{-1}. For the photorheological tests, the instrument was equipped with a quartz bottom plate and a UV lamp (Hamamatsu LC8 lamp, Hamamatsu Photonics) was placed below this latter. A light intensity of 30 mW/cm^2 was set and light was switched on after 60 s, to allow the system to stabilize before the onset of polymerization. The gap between the plates was fixed at 0.3 mm, time sweep measurements were performed during irradiation at a constant frequency of 1 Hz. According to preliminary amplitude sweep tests, the experiments were performed within the linear viscoelastic region (strain amplitude γ of 1%).

Polarized-Light Microscope: the microphotographs were acquired using an Olympus DSX1000 digital microscope, under double-polarized, transmitted light at magnifications ranging from 300X to 800X.

Gel content and swelling: To quantify the covalently crosslinked fraction of the 3D printed material, small pieces were weighted, enveloped in a metal net and immersed in H_2O and DMSO as solvents, in order to solubilize the non-crosslinked fraction. After 24 h the samples were taken out and dried in vacuum at 90 °C overnight. The cross-linked part was calculated gravimetrically, taking into account the ratio of weight after and before the treatment.

To quantify the material's absorption capacity, small pieces were cut,

weighed, and immersed in H_2O and DMSO. After 24 h, the pieces were gently cleaned to remove excess solvent and then immediately weighed to assess their absorption capability and stability in the solvents.

DSC: Differential scanning calorimetry was performed placing about 10 mg of sample in an aluminium crucible. Cooling ramps from RT to −70° C (speed 10° C min^{-1}) were performed on the liquid DESs, a double cooling (−70° C) and heating cycle (80° C) was performed on the CP6 polymer (speed 10° C min^{-1}).

Electromechanical tests: Sensor's electrical and mechanical performances were evaluated through a universal testing machine (FZ3-X500N, Test Engineering) with a load cell of *500 N* coupled with a LCR meter (BK 894, B&K Precision) for the electrical resistance evaluation. Copper strips were employed to acquire the resistance signal. The impedance of the sample was modeled using an equivalent circuit composed of a resistor (R_p) and a capacitor (Cp) connected in parallel. All electrical measurements were carried out with an applied voltage of *0.5 V* and a test frequency of *1000 Hz*. Only the piezoresistive behaviour was explored.

Tensile tests: were performed applying a constant tensile velocity of 10 mm min^{-1} up to 200% of strain. The dumbbell-shaped specimens had nominal dimensions of 30 mm of total length, 12 mm gauge length, 9 mm overall width, 3 mm gauge width, and 3 mm thickness. Strip and mesh samples had nominal dimensions of 15 × 40 × 1.5 mm^3

The cyclic behaviour was evaluated through cyclic tensile test, conducted at 10 mm min^{-1}, with each cycle reaching 50% of strain. A total of 800 subsequent cycles were performed.

Compression tests: were conducted with a constant velocity of 1 mm min^{-1} up to *100 N*. The nominal dimensions of the 3D printed samples were 15x15x9 mm^3.

For each test, the electrical resistance (R_p) was measured. Then, the relative variations of resistance were derived according to the formula:

$$\frac{\Delta R}{R_0} = \frac{R - R_0}{R_0}$$

where R is the resistance at a certain point of the test and R_0 is the resistance when no load is applied.

DMTA: dynamomechanical experiments were carried out using a Triton Technology-TTDMA. Temperature sweep measurements (3° C min^{-1}) were firstly preformed with a constant cyclic tensile deformation of 1% and a constant frequency of 1 Hz to evaluate the Tg of the material and the E' value in the rubbery plateau. The effective crosslinking density of the eutectogel was calculated as $\nu e = E'/3RT$.

where: E' = storage modulus in the rubbery plateau (MPa), R = gas constant = 8.314 J mol^{-1} K^{-1},

T = temperature at which E' is measured (K). Subsequently impedance measurement was coupled to the dynamic-mechanical test. Strips with nominal dimensions 1.50 × 5 × 10 mm^3 were tested by clamping their edges with conductive wires at the DMTA grips, ensuring electrical insulation from the metallic parts of the instrument using polyimide tape. Sample electrical and mechanical response was evaluated in a temperature range from −15 °C to 80 °C, setting a heating rate of 3 °C min^{-1}.

Piezoresistive sensitivity to small tensile deformations was analysed through DMTA analysis performed at RT. Cyclic tensile deformations of 200 μm, 100 μm, 50 μm, 10 μm, 5 μm, 2.5 μm were tested. For each tensile displacement level, the frequency of deformation was varied from 0.1 to 2 Hz to investigate the response dependency on the loading rate. The relative resistance variation for each cycle of the electrical curve was computed according to this formula:

$$\frac{\Delta R}{R_0} = \frac{peak_i - valley_i}{valley_i} \cdot 100$$

where $peak_i$ and $valley_i$ are the i-th peak and valley, respectively, of the sample's cyclic resistance curve, resulting from the cyclic tensile load applied by the DMTA.

For the proof of concept for wearable devices tests, written consent from all participants was obtained prior to the research; no specific risks for the participants were evaluated.

3. Results

3.1. Cellulose extraction and characterization

Dry olive leaves were harvested in local Sardinian olive groves, and these were dried in a vacuum oven to remove all water traces and then ground to obtain a homogeneous powder (average particle size 200 μm). The chemical composition of the leaves was determined and revealed an ash content, i.e., the amount of inorganic components, counting 7.2 wt% with a residual humidity of 3.3 wt%. The amount of fatty acids resulted to be 8.9% while the fibrous components, i.e, cellulose, lignin, and hemicellulose, were detected in the percentages of 10.4%, 23.2% and 7.33%, respectively, indicating that the fibrous fraction, which is the one involved in this work, counts for the 40.9 wt% of the original material. The composition of the leaves powder is in line with other olive leaves data reported in the literature [56–58].

An unbleached-cellulose-pulp extraction procedure was then followed to separate the lipidic fraction and small molecules, and subsequently reduce the amount of lignin and hemicellulose. The FT-IR analysis performed in ATR mode on the extracted powder (Fig. 1, b S1) showed the typical spectrum of cellulose pulp still containing residual lignin and hemicellulose, as well as the possible presence of residual fatty acids. Indeed, ATR showed the presence of characteristic cellulose peaks, while the peak at 1730 cm^{-1} can be attributed to components of lignin and/or hemicelluloses. Additionally, the bands at 2800–2900 cm^{-1}, related to CH and CH_2 stretching in cellulose, hemicellulose, and fatty acids, also decreased, suggesting a reduction in fatty acid and lignin content [59,60]. A more detailed analysis of the ATR spectra is reported in the Supporting Information, where ^{13}C NMR analysis and thermal analysis are also reported (Figs. S1, S2, and S3). Van Soest analysis was also performed on the extracted cellulose pulp showing a total fibrous fraction greater than 85%, with values for cellulose, hemicellulose, and lignin equal to 52.4%, 3.2%, and 29.7%, respectively, confirming the qualitative indications given by NMR and FTIR. XRD analysis (Fig. S4) also revealed an amorphous nature of the pulp given by the presence of hemicellulose and lignin.

SEM images (Fig. 1, c and S4) confirmed the presence of relatively long fibers and particles that could be ascribed to the presence of lignin and hemicellulose that act as cementing material in the natural structure of the leaves, as well as to the presence of residual fatty acids. Despite the presence of particles with different morphology, due to the direct recovery of the material from waste and to the mild treatment performed, cellulose pulp derived from olive leaves is rich in hydroxy-groups. For this reason, a hydrogen-bond scissor (HBS) formulation was developed to disperse and eventually solubilize the different components.

3.2. Preparation of the DES- based formulations

A combination of $ZnCl_2$ dissolved in water and Acrylic Acid (AA) was chosen as the HBS [33], being known the behaviour of this solution as DES [41]. Different molar ratios between the solvent components, i.e. $ZnCl_2$, water, and Acrylic acid, were initially prepared, varying from 1:1:2, 1:1:2.5, 1:1:3, 1:1:3.5 to 1:1:4 respectively.

The viscosity of the different solutions was investigated, showing an increase with the reduction of the molar amount of AA (Fig. 2, a). The preliminary study on the neat DES composition and on their behaviour in the presence of cellulose pulp (6 wt%) is reported and discussed in the Supplementary File. Viscosity and reactivity were evaluated with rheological and photorheological tests (these latter in the presence of BAPO as photoinitiator) as screening characteristics of the formulations, being of high importance in 3D printing. Beside this, higher CP/AA

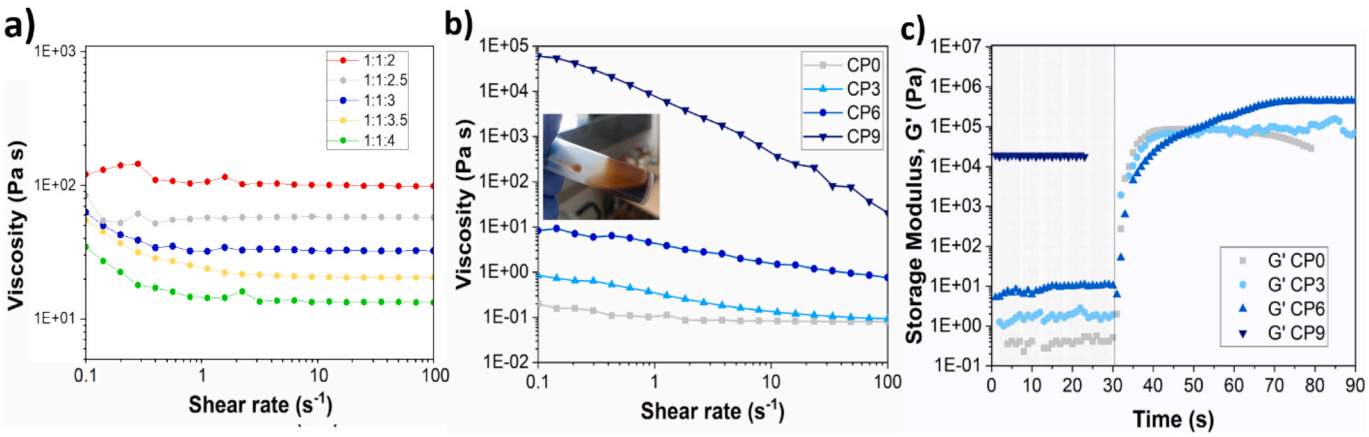


Fig. 2. (a) Viscosity of the ZnCl2:H2O: AA studied solutions; (b)Viscosity of the formulations based on the 1:1:3 DES solution with different amounts of cellulose pulp, inset: image of the stable cellulose pulp dispersion; (c) Photoreheology curves of the formulations based on the 1:1:3 DES solution with different amounts of cellulose pulp, in the presence of 1 wt% of BAPO photoinitiator.

weight ratio were preferred when possible. According to these considerations, the solution 1:1:3 was chosen for further tests.

In parallel, different amounts of cellulose pulp were also tested aiming to evaluate the effect of different CP/AA ratios starting from the 1:1:3 DES solution. Firstly, the visual homogeneity and stability of the prepared formulations, was checked and the evaluation of their viscosity and reactivity, in the presence of the photoinitiator, was again used as preliminary screening for the selection of the best formulation.

To do this, 3, 6, and 9 wt% of cellulose were tested and compared to the solvent mixture without cellulose. The eutectogel samples will be named CP0, CP3, CP6, and CP9. It can be observed an increase in viscosity when the cellulose content is higher (Fig. 2, b); the formulations using 3 and 6 wt% of CP gave a stable and homogeneous fluid while the use of a larger amount of cellulose did not allow its good dispersion, giving a paste-like formulation with high viscosity. Furthermore, an increase in the shear-thinning behaviour can be observed across the whole shear rates when the amount of cellulose is increased. This behaviour can be due to the formation of a highly entangled network or the presence of aggregates and particles [61]. Herein, the presence of residual fibers and the lower solubilization of the aggregates in sample CP9, could increase this effect.

Also the photorheological tests (Fig. 2, c) showed that samples containing up to 6 wt% of CP presented a good reactivity to UV light with an increase of the G' modulus of more than two order of magnitudes in less than 5 s of irradiation and the reaching of the plateau after 12 s for the formulations CP0 and CP3. CP6 showed a slower kinetics after the first seconds, requiring about 40 s to reach the G' plateau. Nevertheless, this latter formulation reached higher values (450 MPa) than the sample with a lower CP amount (88 MPa), indicating the formation of a more rigid network. Instead, the sample containing 9 wt% of CP presented an excessively high G' value even before irradiation indicating that it was not suitable for the photorheology test.

According to the obtained results, deeper studies were conducted on sample CP6; this sample finally presents a CP/AA weight ratio of about 11 indicating that, after curing, the polymeric network consists of 10% CP acting as the crosslinking agent and 90% poly(acrylic acid), within which the salt is dissolved in the presence of a small amount of water.

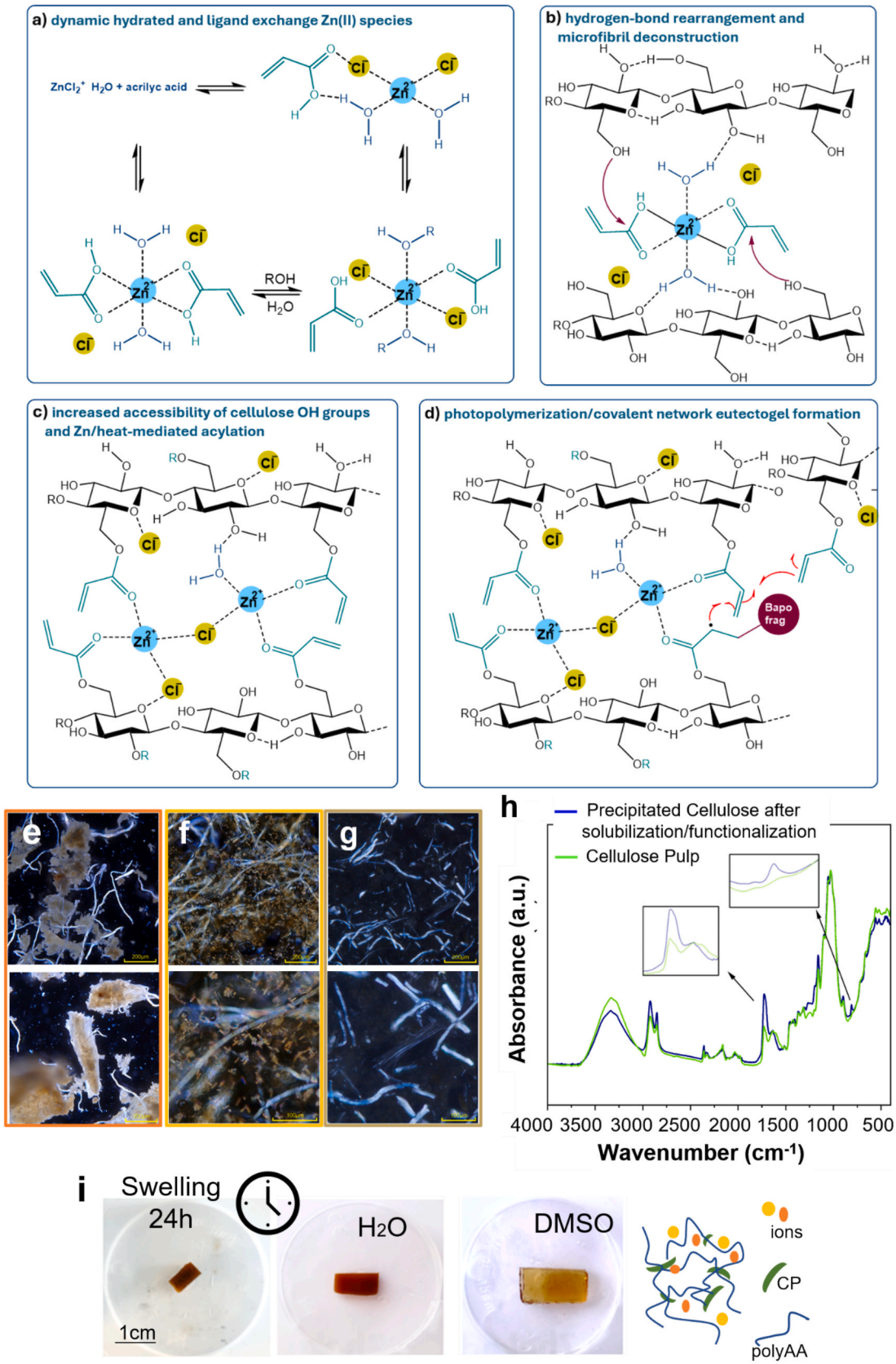
3.3. *Evaluation of the DES-cellulose interaction*

The role of the selected DES on the cellulose structural and chemical modification and the subsequent formation of a crosslinked cellulose-polyAA network is schematically depicted in Fig. 3 a, b, c, d.

Aiming to better understand the interaction between the studied solvent and CP, images were collected using polarized-light microscopy. The cellulose pulp was first observed in the dry state, immediately after its addition to the solvent, and after the complete mixing and heating procedure. As shown in Fig. 3, e, the extracted pulp consists of long fibres with micrometric dimensions together with large micrometric aggregates. After mixing with the solvent, these aggregates are rapidly disrupted, while shorter birefringent fibres remain visible because of the persistence of crystalline domains within the cellulose structure (Fig. 3, f). Similar polarized-light microscopy observations have been reported for cellulose undergoing dissolution or structural disassembly in eutectic and ionic solvents [62,63]. After the complete dispersion procedure, only long residual fibres remain visible, whereas the smaller particles and aggregates disappear, indicating that the cellulose has undergone an extensive structural reorganization while retaining a dispersed fibrous fraction (Fig. 3, g).

These observations suggest that the $ZnCl_2/H_2O$/acrylic acid system does not induce complete molecular dissolution of cellulose [64], but rather promotes fibre swelling, aggregate disassembly, and partial deconstruction of its supramolecular organization, consistent with the behaviour previously reported for hydrated zinc chloride-based DESs under mild processing conditions [33,36,37]. Such behaviour is particularly advantageous for the present application because it exposes a larger fraction of cellulose hydroxyl groups while preserving the reinforcing role of the residual fibres.

The experimental observations, together with previous reports on hydrated $ZnCl_2$-based DESs, suggest that this behaviour arises from the cooperative action of all the components of the eutectic medium. In this highly concentrated ionic environment, Zn(II) is expected to exist as a dynamic population of hydrated and ligand-exchanged species involving water, chloride ions, acrylic acid, and cellulose hydroxyl groups as schematically represented in Fig. 3, a. Owing to its Lewis acidic character and flexible coordination sphere, Zn^{2+} can reversibly interact with oxygen-containing functionalities. These transient interactions, together with the hydrogen-bonding contribution of water and acrylic acid and the strong coordinating ability of chloride ions, are proposed to weaken the extensive intra- and intermolecular hydrogen-bonding network responsible for cellulose crystallinity. Consequently, rather than forming permanent Zn-bridged structures, the solvent establishes a dynamic coordination environment that continuously reorganizes the interactions surrounding the cellulose chains (Fig. 3, b, c), facilitating disruption of the microfibrillar organization, fibre swelling, and aggregate disassembly. Under this mechanistic interpretation, the observations obtained by polarized-light microscopy should not be regarded merely as evidence of physical dispersion, but rather as the manifestation of a structural reorganization that renders cellulose hydroxyl groups chemically accessible for subsequent reactions.



(caption on next page)

Fig. 3. (a) Schematic representation of the hydration equilibria and ligand exchange processes occurring around Zn(II) species in the $ZnCl_2/H_2O$/acrylic acid formulation. Water molecules and acrylate ligands dynamically coordinate the Zn(II) center, generating a distribution of hydrated and mixed-ligand complexes that contribute to the solvent structure and its interaction with cellulose; (b) Zn(II)-mediated reorganization of the hydrogen-bonding network within cellulose fibres, promoting fibre swelling and dispersion while simultaneously enabling the esterification of cellulose hydroxyl groups with acrylic acid to yield acrylate-functionalized cellulose.; (c) acrylic acid-mediated functionalization of cellulose hydroxyl groups through ester bond formation, introducing photocurable acrylate moieties into the cellulose structure; (d) Proposed mechanism for the photopolymerization of acrylate-functionalized cellulose and free acrylic acid, initiated by radical species generated from the homolytic cleavage of BAPO under light irradiation, yielding a crosslinked cellulose-based eutectogel. (e) Images collected with a polarized-light microscope for dry cellulose pulp; (f) cellulose pulp just immersed in the 1:1:3 DES solution; (g) cellulose pulp after the dispersion procedure (scale bar 200 μm upper line, 100 μm lower line); (h) IR spectra of the cellulose pulp precipitated and washed after the dispersion and functionalization procedure in the 1:1:3 solution compared with the extracted cellulose pulp; (i) Swelling in water and DMSO of the photocured CP6 sample (original dimension 0.7 × 1.5 cm) and schematic representation of the composition of the polymerized sample.

The same coordination environment may also account for the simultaneous functionalization of cellulose occurring during the treatment. As hydroxyl groups become progressively exposed, coordination of Zn-containing species to the carbonyl oxygen of acrylic acid may increase the electrophilic character of the carboxylic group [65], facilitating its reaction with cellulose hydroxyl groups (Fig. 3, c, d). The feasibility of cellulose esterification in carboxylic acid-based DESs has previously been demonstrated, supporting the proposed role of the eutectic medium as both a cellulose-processing solvent and a reactive functionalization medium [47]. Under this interpretation, cellulose acrylation is intrinsically coupled to the progressive disruption of the cellulose supramolecular structure: as the hydrogen-bonded network is reorganized and previously buried hydroxyl groups become accessible, the Lewis acidic environment promotes ester-bond formation, enabling the direct generation of acrylic-functionalized cellulose within the same processing step.

To verify this mechanistic hypothesis, the cellulose pulp was precipitated after the mixing and heating treatment in the 1:1:3 DES, extensively washed, and dialyzed. Fig. 3h compares the ATR spectra of the recovered material with that of the untreated cellulose pulp. After treatment, the relative intensity of the carbonyl absorption at approximately 1700 cm^{-1} increased, together with the appearance of a weak band at approximately 810 cm^{-1}, characteristic of acrylic double bonds [55]. These observations were further supported by solid-state ^{13}C NMR analysis, which revealed a degree of substitution of approximately 0.13, as discussed in the Supporting Information (Fig. S8).

The role of heating was subsequently assessed by comparing three formulations: CP6 prepared using the complete mixing and heating procedure, CP6_no_heating prepared without the thermal step, and the cellulose-free formulation CP0. After the addition of BAPO, the formulations were cast, UV-cured for 3 min, and immersed in water or DMSO for 24 h. CP6 maintained its integrity and underwent swelling without losing its shape (Fig. 3 i), confirming the formation of a crosslinked network in which the functionalized cellulose pulp acts as a multifunctional crosslinker. In contrast, both CP6_no_heating and CP0 dissolved in the two solvents, indicating that, in the absence of an effective crosslinker, acrylic acid produces only soluble linear poly(acrylic acid) chains. The dissolution of CP6_no_heating further demonstrates that the interactions established during room-temperature mixing alone are insufficient to generate a stable covalent network. Heating is therefore essential to promote efficient cellulose functionalization, most likely by overcoming the kinetic barrier associated with ester-bond formation. This conclusion is supported by the observation that shorter heating times or lower temperatures did not produce gels capable of retaining their integrity after solvent immersion. Overall, these results support the proposed dual role of the $ZnCl_2/H_2O$/acrylic acid DES: it first acts as a cellulose-processing medium by disrupting the supramolecular hydrogen-bonded architecture through dynamic coordination and hydrogen-bond rearrangement, and subsequently as a reactive medium that promotes cellulose acrylation, enabling its covalent incorporation into the photopolymerized network.

Considering the swelling of sample CP6, this showed an increase in weight of 33% when immersed in water and a much larger increase (300%) when immersed in DMSO. The different behaviour is since water is a good solvent for AA, but cellulose tends to precipitate in this solvent, while DMSO results in a relatively good solvent for both the components of the polymeric network.

3.4. DLP printing

The analyses described so far, defined the protocol for the preparation of a one-pot formulation based on polymerizable DES and cellulose as a crosslinker. The good reactivity and viscosity observed for the formulation endow the possibility to be tested as resin for DLP printing (Fig. 4, a). Furthermore, the cellulose functionalization was crucial to enable the printing with this technique; indeed, without the presence of a crosslinker, the photocured linear polymer would solubilise in the liquid resin in the VAT.

To determine the parameters for the printing process, the curing behaviour of the formulation in the DLP apparatus was tested, and the relationships between curing thickness and the exposure time were evaluated as discussed in the SI [66]. These tests are fundamental for establishing optimal parameters for the printing. Defined values are reported in the Supporting Information file (Fig. S9, Table S2). After performing the preliminary evaluations, different CAD models were designed and reproduced (Fig. 4 and S10). Designs with low-dimensional features were produced to evaluate the printability of the formulation and the spatial resolution that could be reached with this additive manufacturing technology. Small patches with millimetric needles and a benchmark tester were printed and observed with an optical microscope (Fig. 4, b and c). The images show the good fidelity to the original dimension and clearly show the layer-by-layer surface roughness typical of DLP printings obtained from resins with good reactivity. The printing of the benchmark file indicates a good printability for features down to 250 μm. More complex geometries with suspended structures were then designed, the resulting objects were subjected to 3D scan, and the obtained images were overlapped with the original CAD files to evaluate the shape fidelity (Fig. 4, d and e and Fig. S10). Green areas represent good fidelity with an error below 100 μm. Subsequently, dumbbell specimens, honeycomb structures, and meshes were also printed for the functional tests.

To evaluate the good polymerization also after DLP printing, the gel content of the printed samples was evaluated after immersion in water and DMSO for 24 h, resulting in high values of 96%±1.5 and 94%1 respectively. This result confirms the successful crosslinking occurred also with DLP printing. DSC analysis and DMTA performed on the 3D printed samples (Fig. S11) confirm the expected good stability of the material.

The DSC measurement revealed a glass transition temperature (T_g) at about −40 °C and no crystallization /melting peaks, while DMTA showed a tanδ peak, indicating the T_g, according to this kind of measurement, at a higher temperature (−18 °C). The difference is ascribed to the different phenomena measured with the two instruments [67]. Nevertheless, according to both measurements, the material can be tested down to temperatures below 0 °C [35,45,68,69].

The effective crosslinking density of the eutectogel was also estimated from the storage modulus (E′) measured in the rubbery plateau region (50 °C), according to the classical rubber elasticity theory.

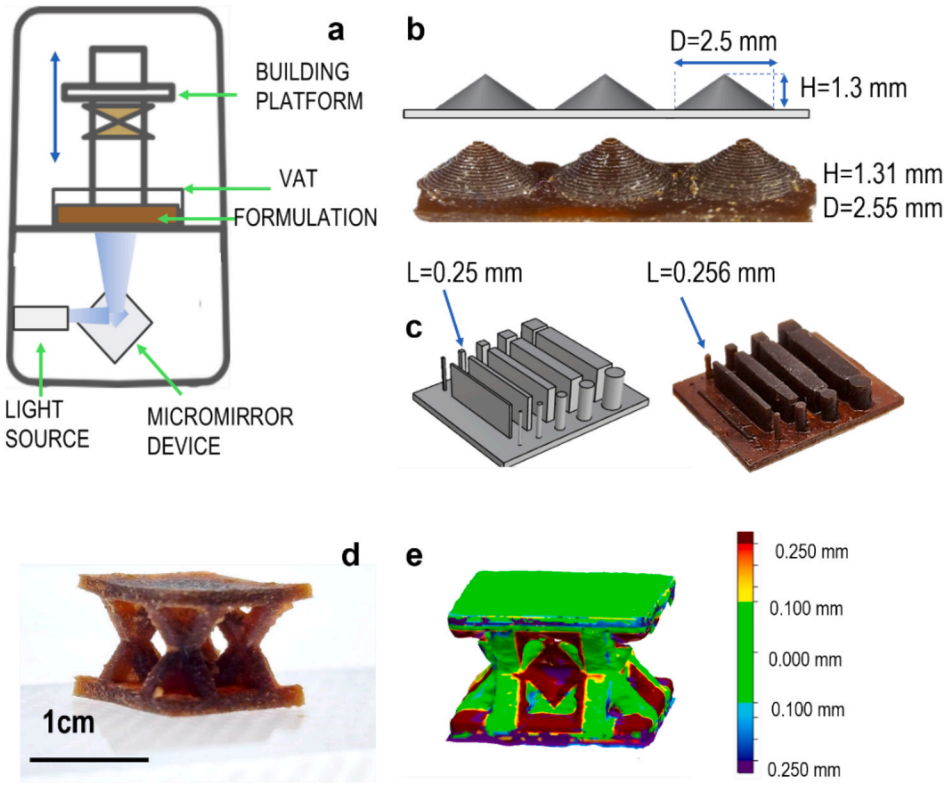


Fig. 4. (a) Scheme of the DLP printer; virtual design and 3D printed reproduction of (b) small patches with millimetric needles and (c) model benchmark; (d) 3D complex structure with millimetric suspended features; (e), color map obtained from the superimposition of the original CAD model and the 3D scan of the printed object.

Considering the measured E′ value of 0.483 MPa, the calculated effective crosslinking density (ν) was approximately 60 mol m^{-3}. This value should be considered as an effective network density rather than a conventional crosslinking density typically evaluated for fully covalent thermosetting networks, since it accounts for the combined contribution of covalent crosslinks, polymer chain entanglements, and reversible ionic interactions acting as additional physical junction points within the network.

To further investigate the contribution of physical interactions to the network structure, the eutectogel was subjected to swelling in DMSO for 24 h, followed by DMTA analysis (Fig. S11). After swelling, the storage modulus decreased to 0.139 MPa, corresponding to an effective crosslinking density of approximately 17 mol m^{-3}. The significant reduction in the calculated network density indicates that DMSO treatment partially disrupts the physical contribution to the network, likely by weakening Zn^{2+}-mediated coordination interactions and reducing secondary intermolecular interactions, while leaving the covalently crosslinked polymer backbone substantially unaffected.

Finally, given the environmental stability of CP6, the structural stability over time was further assessed by DMTA analysis after 20 weeks of storage. The results show that Tg remains nearly unchanged, with only a slight shift from −18 °C to −22 °C, as well as the E' value at the rubbery plateau, suggesting that no significant alterations in the polymer network structure or cross-linking density occur during this storage period (Fig. S11).

3.5. Electromechanical characterization

The prepared samples were then characterized in terms of their mechanical properties. Dumbbell-shaped specimens fabricated via 3D printing were subjected to tensile testing, exhibiting no rupture up to 200% tensile strain (Fig. 5, a, c). An average Young's modulus of 0.47 ± 0.12 MPa was observed, these values differ from other polymerizable DES reported in literature due to the use of the green crosslinker [70] or to the different nature of the DES [71] but they result anyhow of relevant interest, being comparable with the values reported about the human skin [72]. This feature, combined with the optimal deformability are key parameters to ensure a good compliance with soft living tissues.

This material exhibits ionic conductivity thanks to the presence of the salt and, as a consequence, piezoresistivity can be exploited to transduce external mechanical stimuli into measurable variations in electrical parameters. When the material is stretched, the ionic conductivity decreases due to the increase in the conductive path length, ideally following the second Ohm's law ($R = \rho\, l/S$), where R is the sample resistance, ρ is the resistivity of the material, l is the length, and S is the cross section of the sample. Therefore, the CP6 eutectogel displayed an increase in electrical resistance when subjected to tensile loads (Fig. 5, a). The resistance dependency on tensile strains, namely the piezoresistive transfer curve, can be well approximated by two linear regions, the first one up to 50% of strain and the second one from 50% to 200% of strain. The average values R^2 were above 0.99 in both regions, exhibiting 0.997 ± 0.001 in the first range and 0.997 ± 0.003 in the second, indeed. The slope of the linear fitting, referred to as Gauge Factor (GF), indicates sensor sensitivity to external strains. The tested samples exhibited values of 0.84 ± 0.04 and 1.45 ± 0.24, in the two linear ranges, respectively, values in line with the other recently reported eutectogels incorporating cellulose derivatives, used as ionically conductive soft strain sensors (Table S3).

Cyclic tensile test at 50% of strain was also performed to evaluate the repeatability of the CP6 measures. After a few initial conditioning cycles, the eutectogel exhibited a constant mechanical behaviour, indicating a limited mechanical hysteresis (Fig. S12, a). From the electrical point of view, although the sensor exhibited a drift through the prolonged test, mainly due to the uncontrolled environmental conditions of the testing room, the amplitude of the resistance cycles remained approximately constant, indicating an unaltered sensitivity over 800

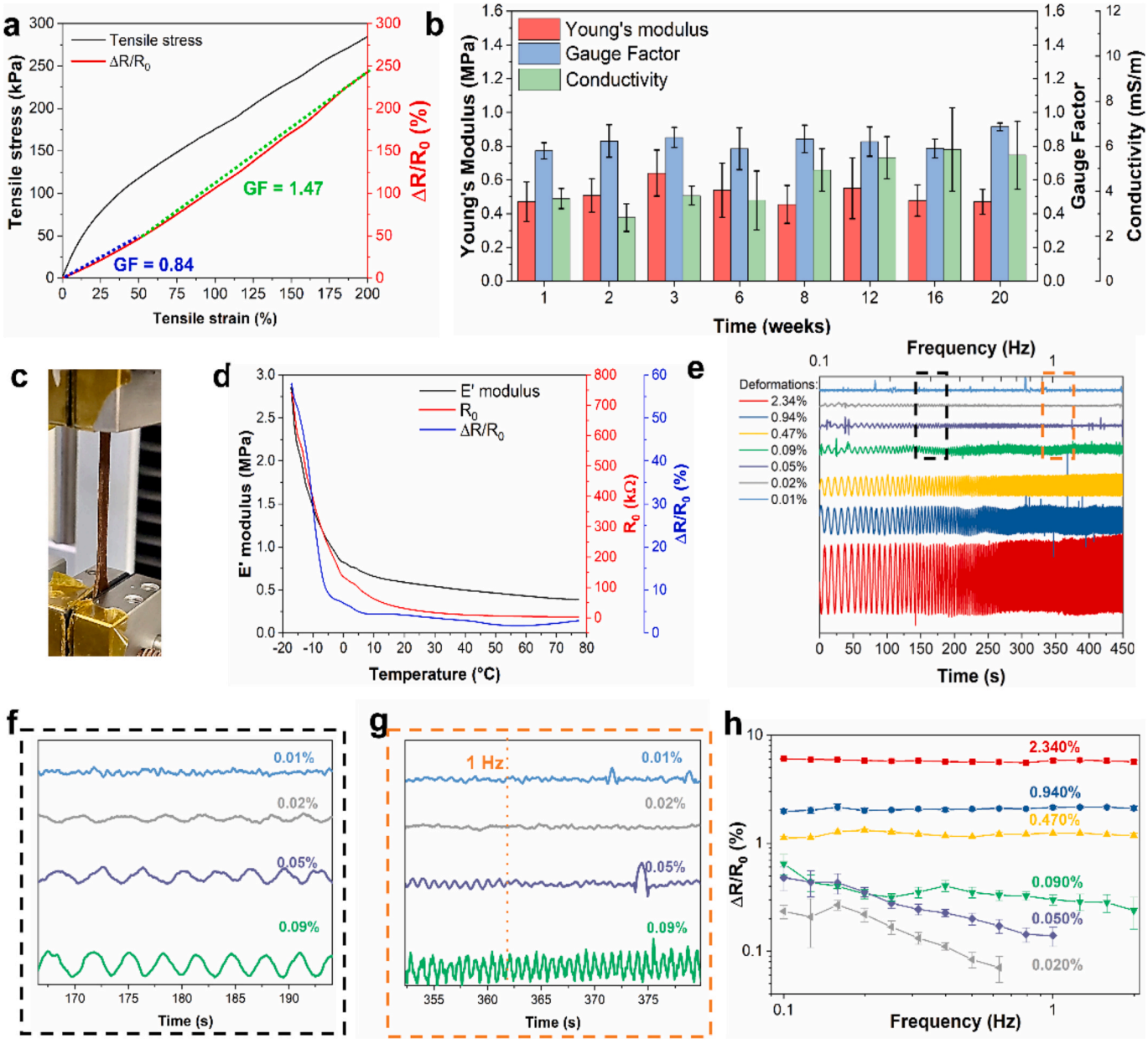


Fig. 5. (a) Tensile stress–strain curves and electrical resistance variation up to 200% tensile strain for CP6 dumbbell-shaped samples. Linear fits are used to evaluate GF in two strain ranges. (b) Young's modulus, gauge factor, and conductivity durability over 5 months; (c) Image of CP6 dumbbell-shaped sample subjected to 200% of tensile strain (d) Young's modulus, electrical resistance and $\Delta R/R_0$ dependency from temperature of a CP6 sample subjected to DMTA test. (e) Electrical resistance response of the CP6 samples under cyclic tensile deformations at different strain and frequencies. Curves were vertically shifted for clarity. Tests were carried out at room temperature. (f,g) Zooms of Fig. 4, e with deformation at frequencies at 0.3 Hz and 1 Hz, respectively. (h) Average $\Delta R/R_0$ obtained from cyclic tensile deformations with amplitudes of 2.34%, 0.94%, 0.47%, 0.09%, 0.05%, 0.02% and 0.01% at frequencies ranging between 0.1 Hz and 2 Hz. The standard deviations are referred to the variability of $\Delta R/R_0$ in cycles at the same frequency.

subsequent cycles (Fig. S12, b).

Moreover, the CP6 eutectogel showed optimal mechanical and electrical stability over time, which is a fundamental feature for sensors that needs to preserve their sensing response [73]. Samples were stored at open-air conditions, without controlling temperature and humidity, for 5 months, and were repeatedly tested using tensile electromechanical measures (Fig. 5, c). Both the stiffness and the GF between 0 and 50% of strain did not show significant changes, remaining stable at approximately 500 kPa and 0.8, respectively, throughout the 20 weeks. This consistency of sensing and mechanical performance of the material is crucial for applications that require medium- to long-term use. In addition, the conductivity of the CP6 eutectogel, initially measured at 4 mS/m, shows a slight increase over time. This behavior may be attributed to gradual moisture uptake from the environment due to the hygroscopic nature of the eutectogel, particularly given by the presence of $ZnCl_2$, as well as to slight corrosion of the copper electrodes used for resistance measurements. Since the samples were stored over 20 weeks under ambient laboratory conditions without controlled temperature or relative humidity, both effects may have contributed to the observed increase in conductivity. However, this effect does not affect the working mechanism of the eutectogel. These results can be attributed to the inherent stability of the DES under ambient conditions and the minimal water content within the polymeric matrix. Unlike conventional hydrogels, where water evaporation significantly limits sensing performance, the water present in this system remains confined and does not readily evaporate, thereby enhancing the long-term reliability and

functionality of the sensor. This exceptional stability, demonstrated across both functional and material properties, largely exceeds that of previously reported cellulose-based eutectogels (Table S3), highlighting the superior durability of the proposed eutectogel under sensing-relevant conditions, while maintaining an optimal balance between sensitivity, flexibility, 3D printability, and high cellulose content. Moreover, as evidenced in the literature analysis of Table S3, in this work the stability of the eutectogel is demonstrated among several different functional parameters, while most of the previous works are focusing only on sample weight variation.

3.6. DMTA-coupled-electrical tests

Owing to the promising thermal properties of the material previously evaluated, the temperature dependence of CP6 eutectogel on the electrical response was investigated. Dynamic mechanical thermal analysis (DMTA) was coupled with the impedance meter to measure electrical resistance of a strip sample under a cyclic tensile strain of 1% at 1 Hz, while the temperature was changed from −15 °C to 80 °C. The test revealed a strong correlation between electrical resistance and temperature. When the temperature is increased, the mobility of ions rises accordingly, leading to a resistance decrease (Fig. S12, c). The cyclic deformation applied by the instrument is consistently reflected in the electrical resistance variations even at subzero temperature, as can be seen in Fig. S12, c and d. Moreover, the Elastic modulus (E') decreased when temperature was increased (Fig. 5, d), due to the enhanced polymeric chain mobility caused by the proximity of the measurement starting temperature with the Tg value. Indeed, above this temperature, chains' relaxation and/or disruption of weak interactions within the matrix occur [74,75]. While stiffness decreased from approximately 3 MPa to about 0.5 MPa in the temperature range investigated, a similar exponential decay trend was observed on R_0, namely the sample resistance when no tensile load is applied, as displayed by the red curve in the same Fig. 5, d. The resistance changed by two orders of magnitude, from roughly 700 kΩ at −15 °C to 3 kΩ at 80 °C, showing the potential of this eutectogel for use as a temperature sensor as well. The resistance decrease is mainly related to the increase of ion mobility with the lowering of the mechanical stiffness. The largest change in resistance is observed in the sub-zero temperature range. Although reduced, the ability to measure electrical resistance and its modulation under mechanical stimuli remains highly interesting for low-temperature applications. In conventional hydrogels, ionic conductivity is almost completely suppressed below 0 °C because of water molecules freezing, and the material behaves as an electrical insulator. In contrast, in eutectogels, ionic mobility decreases in the sub-zero range due to stiffening of the polymer matrix as it approaches the glass transition temperature (Tg ≈ –20 °C). Nevertheless, a measurable electrical resistance is retained, making these materials suitable for sensing applications even at low temperatures.

Since, through the DMTA test, a continuous cyclic tensile deformation is applied to the sample, the resistance cycle amplitude can be derived. In Fig. 5, d the resistance percentage variations relative to the no load resistance (R_0) for each cycle, referred to as cycle amplitude ($\Delta R/R_0$), are displayed by the blue curve. It is clear that the amplitude of cycles in the electrical resistance signal exhibited a pronounced dependence on temperature, when temperature rose, cycles amplitude dropped, following again an exponential decay. It is worth noting that, fixing the applied strain, the resistance cycle amplitude is an indirect indicator of sensor sensitivity. Therefore, the sensitivity of the CP6 eutectogel is lower when the temperature is higher, due to the combined effects of the increased ionic mobility and polymer chains rearrangement. The blue curve can represent an efficient way to represent this correlation, helping in decoupling temperature and strain stimuli.

Strain amplitude and frequency limits of application of the CP6 sensor were investigated by applying small cyclic tensile stimuli of 2.34%, 0.94%, 0.47%, 0.09%, 0.05%, 0.02% and 0.01% at different application frequencies ranging from 0.1 Hz to 2 Hz, with frequencies logarithmically changed. The test was performed at RT, and sensor electrical resistance was continuously measured. The results demonstrated that the sensor could effectively track the external deformations, shown by the amplitude of resistance cycles according to the strain applied (Fig. 5, e). In particular, observing the zoom in Fig. 5, f, it is clear that the minimum strain detectable was 0.02% as it was the last strain where the resistance cycles are still evident. However, increasing the deformation frequency led to a loss of signal resolution, since both 0.02% and 0.05% are no more visible after 1 Hz of deformation, as reported in the zoom in Fig. 5, g. Computing the percentage resistance variations to resistance at no strain applied ($\Delta R/R_0$), and then averaging these values for each application frequency, the Fig. 5, h was derived. It is clear from that figure that sensor response is stable over different application frequencies for higher strain amplitudes. However, the resistance of the sensor did not change consistently for tiny strains, because the resistance cycles are hidden by electrical noise, resulting in a poor distinguishability of the contribution given by the applied strain. Therefore, the CP6 sample exhibited an outstandingly low limit of strain detection of 0.02% at low deformation frequencies, while the detection limit rose to 0.09% for application frequencies up to 2 Hz.

3.7. 3D printed sensors characterization

Given the optimal 3D printability of the CP6 one-pot formulation through the DLP technique, complex geometries, unachievable through the conventional casting technique, were considered to fabricate sensors with enhanced performances. First, two geometries optimized for tensile stress sensing were printed, a solid *stripe* and a *mesh* with an oblique pattern. Both samples display an optimal stretchability, sustaining strains superior to 100% without rupture (Fig. 6, a and b). The *mesh* structure exhibited a lower stiffness compared to the solid *stripe*, as a consequence of the voids within the structure. Therefore, under the same fixed load, the *mesh* underwent greater deformation to the *stripe*. Since resistance variations are strongly dependent upon sensor deformation, it is clear that the more deformable the sensor is, the greater the resistance variations it exhibits under a certain load [76]. Therefore, the *mesh* sensor displayed a greater sensitivity to tensile stresses than the classic *stripe* sensor (Fig. 6, c).

The same concept can be transferred to CP6 polymer 3D samples designed for pressure sensing. *Honeycomb*, *tri-stars*, and *star* patterns were successfully printed with an optimal resolution (Fig. 6, d), and their electromechanical performances were compared to a *bulk* printed sample with the same lateral dimensions. Compressive tests, coupled with electrical resistance measures, were carried out to evaluate their response under applied pressures. From the inset in Fig. 6, e, it is clear that the *honeycomb* is the softest structure, followed by *tri-stars* and *stars,* while the *bulk* structure had the highest Young's modulus. The optimal resolution of the printed structure was once again proved. Bumps in the *stars* and *tri-stars* stress–strain curves can be noticed. They correspond to the various phases of the compression: at the beginning, the voids inside the structures collapsed, and then the structures followed the same behaviour as the bulky one (Fig. 6, e). In the *tri-stars*, the collapsing of the middle void, followed by the collapse of one of the external ones, is slightly visible as a change in the slope at 20% and 40% of strain, respectively. This can be seen in Movies 1 and 2, where the stars and *tri-stars* were compressed to approximately 80% of their thickness, returning to their original shape without damage. This stepped effect was not observed in the honeycomb structure, due to the more homogeneous distribution of the voids in the lattice.

The electrical resistance of the samples was measured in real-time during the mechanical compression. Resistance values were normalized to the resistance value under no-pressure conditions. All 3D printed samples showed a decrease in resistance under increasing compressive load, because of the shortening of the ionic conduction path between the two electrodes, one placed on the upper surface of the sample and the

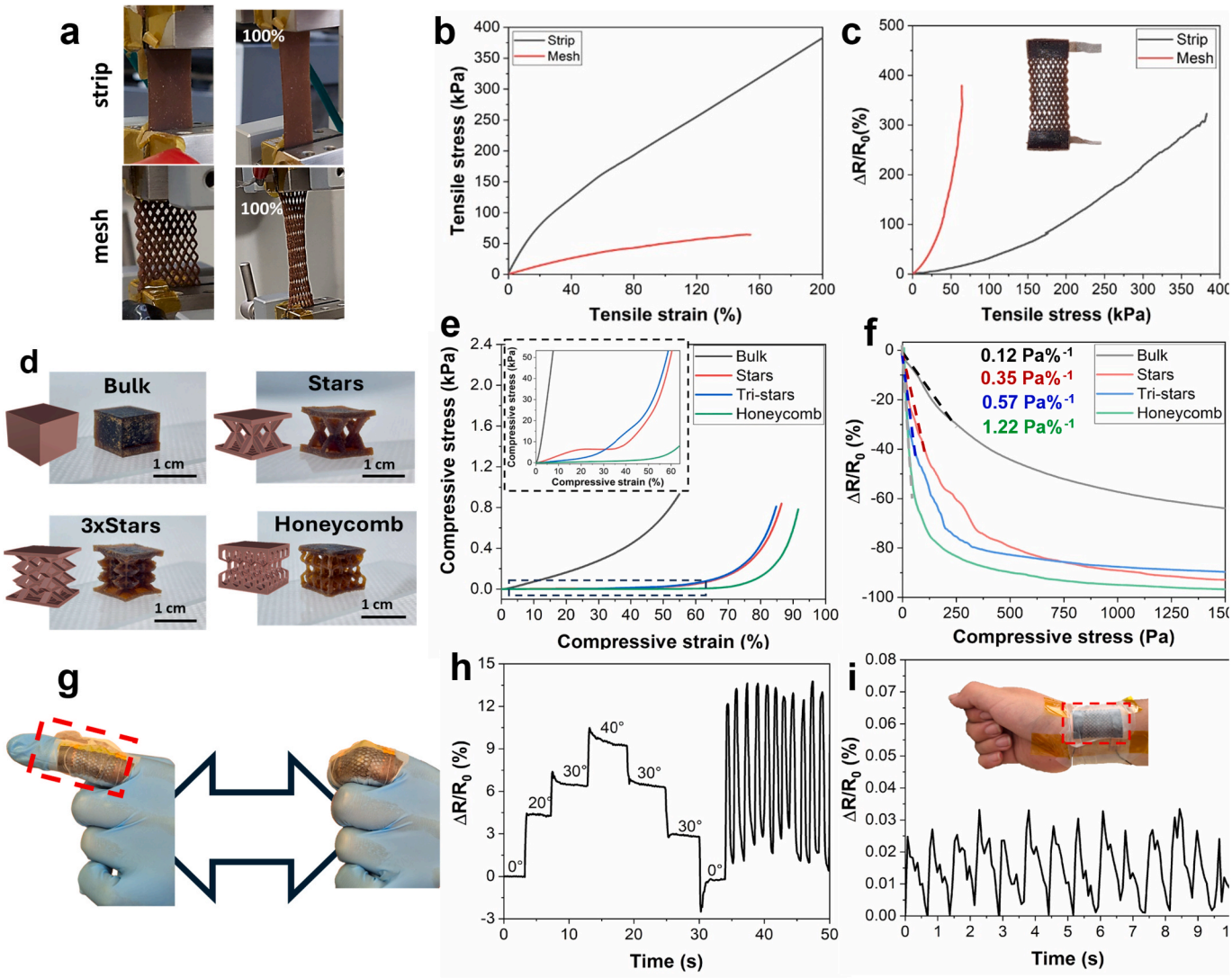


Fig. 6. (a) Image of 3D printed strip and mesh samples at rest and under a 100% tensile deformation. (b) Tensile stress–strain curves and (c) related electrical resistance variation under tensile stress of strip and mesh samples (Inset: Mesh specimen width: 2.3 cm). (d) CAD and images of the four 3D-printed geometry used to fabricate compressive stress sensors. (e) Compressive stress–strain curves and (f) related electrical resistance variation under tensile stress of the different 3D printed sample. Linear fits are used to evaluate pressure sensitivity reported in the graph (g) Images of the mesh samples mounted on a finger to detect finger bending. (h) Electrical resistance variation of mesh sample during finger bending at different angle and velocity. (i) Electrical resistance variation of mesh sample while monitoring heart pulse wave sensed from the wrist.

other on the bottom. Samples exhibited a rapid resistance drop under small pressures, followed by a saturation region, where the resistance remained nearly constant despite the load continuing to increase (Fig. S13, a). In the low-pressure region, the 3D printed architectures displayed a higher sensitivity than the bulk geometry, as can be seen by the linear fitted curves in Fig. 6, f. In particular, the softer the structure, the more sensitive it is to applied pressure loads. The *honeycomb* architecture exhibited a 10-fold increase of sensitivity for pressure below 50 Pa to bulk, indeed. However, the resistance response of these complex geometries is sharper at tiny loads, leading to a saturation at lower compressive forces and thus limiting their effective application range. This is clearly illustrated by the pressure regions where sensitivity was computed, reported in the table in Fig. S13, b. From these examples, it is evident that 3D printing represents a powerful and innovative technique to tailor mechanical and sensing performances of strain sensors to meet the requirements of different final applications.

As a proof of concept, the 3D printed mesh architecture was fixed onto the finger of a volunteer to demonstrate the applicability of CP6 eutectogel as a sensor for joint motion recognition (Fig. 6, g). The index finger was bent, and the sensor, placed between the proximal phalanx and the middle one, exhibited measurable resistance changes. The resistance curve showed a good stability across different bending angles (Fig. 6, h), demonstrating that, with proper calibration, the sensor response can be reliably associated with joint motion. This was further demonstrated by repetitive finger bending performed just after angle measurements: the mesh sensor displayed a good repeatability across the subsequent bending cycles (Fig. 6, h).

Moreover, the exceptionally low strain limit of detection of CP6 polymer was proved by measuring the arterial pulse wave at the wrist. A heartbeat of 84 bpm was recorded, and the resistance signal exhibited a good fidelity in the pulse wave at the wrist comparable with the reported signals in literature [77] (Fig. 6, i).

The ability to sense both small and large deformations with good repeatability, combined with the optimal durability, flexibility, and tailorability given by 3D printing, makes the proposed material an optimal choice to improve remote healthcare and sports medicine. Nevertheless, further investigations are required to validate its performance under realistic wearing conditions, such as stability in the

presence of sweat, and to assess its biocompatibility for long-term skin-contact applications. The same features point out its potential integration in soft robots or as a functional substrate for human–machine interface development, using waste materials and representing a greener alternative compared to the conventional crosslinked materials used for strain sensing. Furthermore, the same approach can be applied to microcrystalline cellulose and cellulose pulp extracted from different sources; preliminary investigations in this regard are ongoing (Fig. S14) and will be the focus of further studies.

4. Conclusions

This work demonstrates a material design strategy for the development of sustainable, printable, and conductive eutectogels by integrating biomass-derived cellulose into a reactive deep eutectic solvent (DES) system.

Interestingly, rather than acting as an inert reinforcing phase, cellulose actively participates in the formation of the polymer network through acrylic acid grafting, while the DES simultaneously provides cellulose dispersion, partial dissolution, functionalization, and a polymerizable medium. This multifunctional approach enables the direct conversion of a lignocellulosic waste-derived material into an active structural component of the final eutectogel.

Cellulose pulp isolated from olive leaves was employed as a locally available agricultural waste, demonstrating its successful valorization into a high-value functional material. The laboratory-scale extraction procedure was intended to provide a representative biomass feedstock which was characterized, highlighting the feasibility of the proposed material design concept.

The resulting reactive formulation, studied to incorporate the highest amount of bio-derived Cellulose Pulp, proved to be well suited for DLP 3D printing, enabling the fabrication of complex architectures with high printing fidelity while preserving high deformability, ionic conductivity, and long-term stability. The combination of these properties enabled the realization of flexible strain sensors capable of detecting strains below 0.01% over a broad operating temperature range. Furthermore, the design freedom provided by additive manufacturing allowed the sensing performance to be tailored through structural geometry rather than changes in material composition.

Overall, this work establishes a versatile platform for the design of biomass-derived multifunctional eutectogels by coupling reactive DES chemistry with additive manufacturing. Beyond the specific material presented here, the proposed strategy offers a general framework for transforming renewable cellulose resources into customizable soft electronic materials, opening new opportunities for sustainable material design within a circular economy perspective. Furthermore and importantly, the preliminary results presented in this work indicate that the same strategy can be extended to cellulose obtained from different sources, suggesting that the approach is not limited to olive leaf-derived cellulose.

CRediT authorship contribution statement

Maria Vittoria Piras: Writing – original draft, Investigation. **Giorgio Mogli:** Writing – original draft, Investigation. **Francesco Corrias:** Supervision, Investigation. **Sara Paniziutti:** Investigation. **Franco Frau:** Methodology. **Giorgia Sarais:** Data curation. **Francesco Secci:** Supervision, Data curation. **Stefano Stassi:** Writing – review & editing, Funding acquisition, Conceptualization. **Annalisa Chiappone:** Writing – review & editing, Project administration, Conceptualization.

Declaration of competing interest

The authors declare the following financial interests/personal relationships which may be considered as potential competing interests: Annalisa Chiappone reports financial support was provided by Italian Ministry of University and Research. If there are other authors, they declare that they have no known competing financial interests or personal relationships that could have appeared to influence the work reported in this paper.

Acknowledgments

The authors acknowledge support from the University of Cagliari under Open Access funding call for the publication of this work.

AC Aknowledges the Ministero dell'Università e della Ricerca (MUR), through PRIN 2022 - PASSO Prot.20222TKNRJ grant and Cascade call for industry and university - PNC0000001_Project INC 3D_Università di Cagliari from National Plan for Complementary Investments to the NRRP, project "D3-4Health - Digital Driven Diagnostics, prognostics and therapeutics for sustainable Health care"

Dr. Dario Fancello is acknowledged for the help with the polarized light microscopy investigation.

Author agreement

All the Authors certify that they have seen and approved the final version of the manuscript being submitted. They warrant that the article is the authors' original work, hasn't received prior publication and isn't under consideration for publication elsewhere.

Appendix A. Supplementary data

Supplementary data to this article can be found online at https://doi.org/10.1016/j.matdes.2026.117016. Supplementary data contains: Analysis on Olive Leaves and Cellulose Pulp, Detailed description of the study of cellulose pulp dispersion and functionalization. 3D printing details and the characterization of the 3D printed polymer.

Data availability

Data will be made available on request.

References

[1] Y. Li, N. Bai, Y. Chang, Z. Liu, J. Liu, X. Li, et al., Flexible iontronic sensing, Chem. Soc. Rev. 54 (10) (2025) 4651–4700.
[2] D. Xu, P. Zhou, J. Wu, G. Xiang, Y. Zhong, H. Guo, et al., Recent progress in high-performance flexible pressure sensors: materials, design, fabrication, and applications, Adv. Mater. Technol. (2025) 2500192.
[3] H. Jin, W. Wang, S. Chen, G. Zhang, Y. Tong, D. Lu, et al., Flexible wearable sensors for sports training: recent advances and future perspectives, Mater. Des. 265 (2026) 115994.
[4] L. Shi, J. Feng, Y. Zhu, F. Huang, K. Aw, A review of flexible strain sensors for walking gait monitoring, Sens. Actuators Phys. 377 (2024) 115730.
[5] J. Wang, Y. Chen, S. Tu, X. Cui, J. Chen, Y. Zhu, Recent advances in flexible iontronic pressure sensors: materials, microstructure designs, applications, and opportunities, J. Mater. Chem. C 12 (36) (2024) 14202–14221.
[6] G. Mogli, M. Reina, A. Chiappone, A. Lamberti, C.F. Pirri, I. Roppolo, et al., Self-powered integrated tactile sensing system based on ultrastretchable, self-healing and 3D printable ionic conductive hydrogel, Adv. Funct. Mater. 34 (7) (2024) 2307133.
[7] Q. Wang, J. Xu, S. Yang, X. Hu, H. Ding, X. Liang, Q. Liu, C. Pang, M. Wang, A superior environmentally stable, sensitive, and low hysteretic graphene foam-based skin-like strain sensor for wearable applications, Mater. Des. 255 (2025) 114191.
[8] H. Wang, Z. Li, Z. Liu, J. Fu, T. Shan, X. Yang, et al., Flexible capacitive pressure sensors for wearable electronics, J. Mater. Chem. C 10 (5) (2022) 1594–1605.
[9] S. Zhao, D. Liu, F. Yan, Wearable resistive-type stretchable strain sensors: materials and applications, Adv. Mater. 37 (5) (2025) 2413929.
[10] C. Hegde, J. Su, J.M.R. Tan, K. He, X. Chen, S. Magdassi, Sensing in soft robotics, ACS Nano 17 (16) (2023) 15277–15307.
[11] Z. Hui, L. Zhang, G. Ren, G. Sun, H.D. Yu, W. Huang, Green flexible electronics: natural materials, fabrication, and applications, Adv. Mater. 35 (28) (2023) 2211202.
[12] K.B.R. Teodoro, R.C. Sanfelice, F.L. Migliorini, A. Pavinatto, M.H.M. Facure, D. S. Correa, A review on the role and performance of cellulose nanomaterials in sensors, ACS Sens. 6 (7) (2021) 2473–2496.

[13] W. Wang, S. Yang, K. Ding, L. Jiao, J. Yan, W. Zhao, et al., Biomaterials- and biostructures inspired high-performance flexible stretchable strain sensors: a review, Chem. Eng. J. 1 (425) (2021) 129949.
[14] N. Nath, S. Chakroborty, D.P. Vishwakarma, G. Goga, A.S. Yadav, R. Mohan, Recent advances in sustainable nature-based functional materials for biomedical sensor technologies, Environ. Sci. Pollut. Res. 31 (46) (2024) 57289–57313.
[15] Z. Zhang, B. Feng, J. Yan, W. Zhao, J. Sun, Advances in bio-based wearable flexible sensors, Green Chem. 27 (6) (2025) 1604–1619.
[16] L. Wang, L. Cao, J. Fan, J. Zhang, C. Ma, Z. Han, Biomaterial-based flexible stretchable sensor devices: classification, composition and their multifunctional integrated applications, J. Bionic Eng. 22 (1) (2025) 12–46.
[17] M. Zhang, T. Xu, K. Liu, L. Zhu, C. Miao, T. Chen, et al., Modulation and mechanisms of cellulose-based hydrogels for flexible sensors, SusMat 5 (1) (2025) e255.
[18] Z. Chen, T. Yan, Z. Pan, Review of flexible strain sensors based on cellulose composites for multi-faceted applications, Cellulose 28 (2) (2021) 615–645.
[19] Y. Zou, Z. Liao, R. Zhang, S. Song, Y. Yang, D. Xie, et al., Cellulose nanofibers/liquid metal hydrogels with high tensile strength, environmental adaptability and electromagnetic shielding for temperature monitoring and strain sensors, Carbohydr. Polym. 348 (2025) 122788.
[20] D. Fu, L. Xing, Y. Xie, P. Li, F. Yang, X. Sui, et al., Hybrid crosslinking cellulose nanofibers-reinforced zwitterionic poly (ionic liquid) organohydrogel with high-stretchable, anti-freezing, anti-drying as strain sensor application, Carbohydr. Polym. 1 (353) (2025) 123253.
[21] H. Sun, Y. Han, M. Huang, J. Li, Z. Bian, Y. Wang, et al., Highly stretchable, environmentally stable, self-healing and adhesive conductive nanocomposite organohydrogel for efficient multimodal sensing, Chem. Eng. J. 480 (2024) 148305.
[22] H. Du, Z. Cheng, Y. Liu, M. Hu, M. Xia, X. Sun, et al., Polydopamine-modified cellulose nanofiber composite hydrogel with strong toughness and high adhesion for human motion detection and wireless sensing, Cellulose 31 (10) (2024) 6421–6433.
[23] D. Xie, M. Li, N. Zhao, M. Wang, Z. Luo, Superior stretchable, strongly adhesive, and environmentally stable multifunctional eutectogel enabled by dual-network and metal-ion coordination strategy, Mater. Des. 1 (264) (2026) 115760.
[24] F. Lin, W. Yang, B. Lu, Y. Xu, J. Chen, X. Zheng, et al., Muscle-inspired robust anisotropic cellulose conductive hydrogel for multidirectional strain sensors and implantable bioelectronics, Adv. Funct. Mater. 35 (10) (2025) 2416419.
[25] H. Zhang, D. Zhang, H. Cai, Y. Ma, K. Li, P. Zhang, et al., A bacterial cellulose-based multifunctional conductive hydrogel for flexible strain sensors and supercapacitors, Carbohydr. Polym. 15 (360) (2025) 123601.
[26] B. Dong, D. Yu, P. Lu, Z. Song, W. Chen, F. Zhang, et al., TEMPO bacterial cellulose and MXene nanosheets synergistically promote tough hydrogels for intelligent wearable human-machine interaction, Carbohydr. Polym. 326 (2024 Feb) 121621.
[27] C. Jiang, C. Zhou, W. Tang, G. Chen, S.N. Yin, W. Xie, et al., Crosslinking of bacterial cellulose toward fabricating ultrastretchable hydrogels for multiple sensing with high sensitivity, ACS Sustain. Chem. Eng. 11 (31) (2023) 11548–11558.
[28] C. Yang, C. Ji, F. Guo, H. Mi, Y. Wang, J. Qiu, Wireless sensor system based on organohydrogel ionic skin for physiological activity monitoring, ACS Appl. Mater. Interfaces 16 (19) (2024) 25181–25193.
[29] G. Mogli, A. Chiappone, A. Sacco, C.F. Pirri, S. Stassi, Ultrasensitive piezoresistive and piezocapacitive cellulose-based ionic hydrogels for wearable multifunctional sensing, ACS Appl. Electron. Mater. 5 (1) (2023) 205–215.
[30] N. Mohd, S.F.S. Draman, M.S.N. Salleh, N.B. YusofB. Dissolution of cellulose in ionic liquid: a review. AIP Conf. Proc. 24 February 2017; 1809 (1): 020035.
[31] Y.L. Chen, X. Zhang, T.T. You, F. Xu, Deep eutectic solvents (DESs) for cellulose dissolution: a mini-review, Cellulose 26 (1) (2019) 205–213.
[32] Q. Zhang, E. Zhu, T. Li, L. Zhang, Z. Wang, High-value utilization of cellulose: intriguing and important effects of hydrogen bonding interactions–a mini-review, Biomacromolecules 25 (10) (2024) 6296–6318.
[33] Z. Tong, J. Meng, S. Liu, Y. Liu, S. Zeng, L. Wang, et al., Room temperature dissolving cellulose with a metal salt hydrate-based deep eutectic solvent, Carbohydr. Polym. 15 (272) (2021) 118473.
[34] A. Khalid, S. Tahir, A.R. Khalid, M.A. Hanif, Q. Abbas, M. Zahid, Breaking new grounds: metal salts based-deep eutectic solvents and their applications- a comprehensive review, Green Chem. 26 (5) (2024) 2421–2453.
[35] J. Płotka-Wasylka, M. De La Guardia, V. Andruch, M. Vilková, Deep eutectic solvents vs ionic liquids: similarities and differences, Microchem. J. 159 (2020) 105539.
[36] Z. Tong, W. Wang, S. Zeng, Y. Sun, J. Meng, Y. Liu, et al., Hydrogen bond reconstruction strategy for eutectic solvents that realizes room-temperature dissolution of cellulose, Green Chem. 24 (22) (2022) 8760–8769.
[37] F. Tamaddon, H. Rashidi, $ZnCl_2$:2HOAc: a deep eutectic solvent for the Friedel–Crafts acetylation of poly-phenols and chemo-selective protection of alcohols, Res. Chem. Intermed. 49 (8) (2023) 3589–3603.
[38] W.J. Huang, T.H. Vo, Y.J. Sheng, H.K. Tsao, Stretchable and conductive physical eutectogel based on type IV deep eutectic solvent through cation-bridging, J. Mol. Liq. 396 (2024) 124011.
[39] R. Wang, Y. Ma, P. Chen, L. Sun, Y. Liu, C. Gao, A double network conductive gel with robust mechanical properties based on polymerizable deep eutectic solvent, Colloids Surf. Physicochem. Eng. Asp. 656 (2023) 130349.
[40] Y. Tian, L. Zhang, X. Li, M. Yan, Y. Wang, J. Ma, et al., Compressible, anti-freezing, and ionic conductive cellulose/polyacrylic acid composite hydrogel prepared via AlCl3/$ZnCl_2$ aqueous system as solvent and catalyst, Int. J. Biol. Macromol. 253 (2023) 126550.
[41] J. Zhu, C. Shao, S. Hao, K. Xue, J. Zhang, Z. Sun, et al., Green synthesis of multifunctional cellulose-based eutectogel using a metal salt hydrate-based deep eutectic solvent for sustainable self-powered sensing, Chem. Eng. J. 506 (2025) 159636.
[42] S. Yao, B. Zhang, S. Hu, H. Zhu, H. Hu, K. Chen, et al., Phase-separated ductile eutectogels with excellent environmental durability and antibacterial features for thermoelectric response and highly sensitive wearable sensors, Chem. Mater. 37 (18) (2025) 7064–7078.
[43] S. Yao, S. Hu, B. Zhang, K. Chen, D. Li, Y. Shang, et al., Bioinspired multifunctional eutectogels for skin-like flexible strain sensors with potential application in deep-learning handwriting recognition, Langmuir 41 (37) (2025 Sep 23) 25349–25359.
[44] X.F. Zhang, X. Ma, T. Hou, K. Guo, J. Yin, Z. Wang, et al., Inorganic salts induce thermally reversible and anti-freezing cellulose hydrogels, Angew. Chem. Int. Ed. 58 (22) (2019) 7366–7370.
[45] X. Sui, H. Guo, C. Cai, Q. Li, C. Wen, X. Zhang, et al., Ionic conductive hydrogels with long-lasting antifreezing, water retention and self-regeneration abilities, Chem. Eng. J. 419 (2021) 129478.
[46] P.A. Mercadal, A. González, A. Beloqui, L.C. Tomé, D. Mecerreyes, M. Calderón, et al., Eutectogels: the multifaceted soft ionic materials of tomorrow, JACS Au 4 (10) (2024) 3744–3758.
[47] S. Liu, Q. Zhang, S. Gou, L. Zhang, Z. Wang, Esterification of cellulose using carboxylic acid-based deep eutectic solvents to produce high-yield cellulose nanofibers, Carbohydr. Polym. 251 (2021) 117018.
[48] Y. Bai, X.F. Zhang, Z. Wang, T. Zheng, J. Yao, Deep eutectic solvent with bifunctional Brønsted-Lewis acids for highly efficient lignocellulose fractionation, Bioresour. Technol. 347 (2022) 126723.
[49] T. Xiao, M. Hou, X. Guo, X. Cao, C. Li, Q. Zhang, et al., Recent progress in deep eutectic solvent(DES) fractionation of lignocellulosic components : a review, Renew. Sustain. Energy Rev. 192 (2024) 114243.
[50] E.L. Smith, A.P. Abbott, K.S. Ryder, Deep eutectic solvents (DESs) and their applications, Chem. Rev. 114 (21) (2014) 11060–11082.
[51] W. Zhao, Z. Wang, J. Zhang, X. Wang, Y. Xu, N. Ding, et al., Vat photopolymerization 3D printing of advanced soft sensors and actuators: from architecture to function, Adv. Mater. Technol. 6 (8) (2021) 2001218.
[52] X. Du, X. Zhang, Z. Zhao, Y. Rong, P. Cui, X. Huang, DLP printing eutectic gels crosslinked by dopamine-grafted nano-cellulose for flexible wearable devices, J. Polym. Sci. 63 (2025) 998–1009.
[53] H. Liu, H. Zhang, W. Han, H. Lin, R. Li, J. Zhu, et al., 3D printed flexible strain sensors: from printing to devices and signals, Adv. Mater. 33 (8) (2021) 2004782.
[54] Y. Li, Y. Liu, S.R.A. Bhuiyan, Y. Zhu, S. Yao, Printed strain sensors for on-skin electronics, Small Struct. 3 (2) (2022) 2100131.
[55] M.C. Cabua, M.V. Piras, D. Dessi, G. Sarais, F. Corrias, M. Zanon, et al., Microcrystalline cellulose from aloe plant waste as a platform for green materials: preparation, chemical functionalization, and application in 3D printing, ACS Appl. Polym. Mater. 6 (12) (2024) 6926–6936.
[56] A. Garcia-Maraver, D. Salvachúa, M.J. Martínez, L.F. Diaz, M. Zamorano, Analysis of the relation between the cellulose, hemicellulose and lignin content and the thermal behavior of residual biomass from olive trees, Waste Manage. 33 (11) (2013) 2245–2249.
[57] S. Sisodiya, M. Debnath, D. Jain, S.S. Shekhawat, An integrated approach using morphological, biochemical, and RAPD markers to assess the genetic diversity of Olive (Olea Europaea L.) cultivars in India, Sci. Rep. 15 (1) (2025) 18664.
[58] A. Lama-Muñoz, C.M. Del Mar, F. Espínola, M. Moya, I. Romero, E. Castro, Characterization of the lignocellulosic and sugars composition of different olive leaves cultivars, Food Chem. 329 (2020) 127153.
[59] L.K. Kian, N. Saba, M. Jawaid, H. Fouad, Characterization of microcrystalline cellulose extracted from olive fiber, Int. J. Biol. Macromol. 156 (2020) 347–353.
[60] J. Lehto, J. Louhelainen, T. Kłosińska, M. Drożdżek, R. Alén, Characterization of alkali-extracted wood by FTIR-ATR spectroscopy, Biomass Convers Biorefinery. 8 (4) (2018) 847–855.
[61] X. Tan, X. Li, L. Chen, F. Xie, Solubility of starch and microcrystalline cellulose in 1-ethyl-3-methylimidazolium acetate ionic liquid and solution rheological properties, Phys. Chem. Chem. Phys. 18 (39) (2016) 27584–27593.
[62] F.H.B. Sosa, R.M. Dias, A.M. da Costa Lopes, J.A.P. Coutinho, M.C. da Costa, Fast and efficient method to evaluate the potential of eutectic solvents to dissolve lignocellulosic components, Sustainability 12 (8) (2020) 3358.
[63] L. Villar, M. Pita, J. Paez, P.B. Sánchez, Dissolution kinetics of cellulose in ionic solvents by polarized light microscopy, Cellulose 30 (5) (2023) 3027–3039.
[64] Y. Xi, L. Zhang, Y. Tian, J. Song, J. Ma, Z. Wang, Rapid dissolution of cellulose in an AlCl3/ZnCl2 aqueous system at room temperature and its versatile adaptability in functional materials, Green Chem. 24 (2) (2022) 885–897.
[65] K.F. Fazende, M. Phachansitthi, J.D. Mota-Morales, J.A. Pojman, Frontal polymerization of deep eutectic solvents composed of acrylic and methacrylic acids, J. Polym. Sci. Part A Polym. Chem. 55 (2017) 4046–4050.
[66] M. Gastaldi, C.A. Spiegel, C. Vazquez-Martel, C. Barolo, I. Roppolo, E. Blasco, 4D printing of light activated shape memory polymers with organic dyes, Mol. Syst. Des. Eng. 8 (3) (2023) 323–329.
[67] M.G. Abiad, O.H. Campanella, M.T. Carvajal, Assessment of thermal transitions by dynamic mechanical analysis (DMA) using a novel disposable powder holder, Pharmaceutics 2 (2) (2010) 78–90.
[68] H. Wu, Z. Pang, L. Ji, X. Pang, Y. Li, X. Yu, Strong adhesive, high conductive and environmentally stable eutectogel based on “water in deep eutectic solvent”: ultrasensitive flexible temperature and strain sensors, Chem. Eng. J. 497 (2024) 154883.
[69] W. Chen, W. Sun, J. Li, Y. Qiu, L. Qiu, J. Ma, et al., multifunctional conductive elastomers based on tannic acid and polymerizable 1-butyl-3-methylimidazolium

chloride/acrylic acid deep eutectic solvent, ACS Appl. Polym. Mater. 6 (1) (2024) 180–191.
[70] G. Zhu, et al., Dye-free and reprintable multi-color DLP 3D printing using $ZnCl_2$-based polymerizable deep eutectic solvents and type I photoinitiators, Chem. Eng. J. 472 (2023) 144987, https://doi.org/10.1016/j.cej.2023.144987.
[71] Z. Wei, et al., Environmentally tolerant multifunctional eutectogel for highly sensitive wearable sensors, Mater. Horiz. 12 (8) (2025) 2604–2618, https://doi.org/10.1039/D4MH01665C.
[72] T. Li, H. Qi, C. Zhao, Z. Li, W. Zhou, G. Li, et al., Robust skin-integrated conductive biogel for high-fidelity detection under mechanical stress, Nat. Commun. 16 (1) (2025) 88.
[73] G. Mogli, I. Roppolo, A. Chiappone, S. Stassi, Multi-responsive 3D printable organohydrogel for the fabrication of durable and low-hysteresis flexible sensors, Appl. Mater. Today 1 (44) (2025) 102675.
[74] Y. Tang, Z. Yu, L. Tam, A. Zhou, D.M. Li, Behaviors of water molecules in polyvinyl alcohol gel amid stretch and temperature changes: a molecular dynamics study, Mater. Today Commun. 1 (33) (2022) 104834.
[75] X. Hu, M. Vatankhah-Varnoosfaderani, J. Zhou, Q. Li, S.S. Sheiko, Weak hydrogen bonding enables hard, strong, tough, and elastic hydrogels, Adv. Mater. 27 (43) (2015) 6899–6905.
[76] A.P. Avolio, M. Butlin, A. Walsh, 3D-printable biocompatible, self-adhesive and long-term stable organohydrogel for wearable sensors, Appl. Mater. Today 49 (2026) 103148.
[77] A.P. Avolio, M. Butlin, A. Walsh, Arterial blood pressure measurement and pulse wave analysis—their role in enhancing cardiovascular assessment, Physiol. Meas. 31 (1) (2009) R1.